Science Bulletin 64 (2019) 44–53

Contents lists available at ScienceDirect

Science Bulletin

journal homepage: www.elsevier.com/locate/scib

Article

Facile synthesis of bimodal macroporous g-C_3N_4/SnO_2 nanohybrids with enhanced photocatalytic activity

Yingzhi Chen [a], Wenhao Li [a], Dongjian Jiang [a], Kuo Men [b], Zhen Li [a], Ling Li [a], Shizheng Sun [a], Jingyuan Li [a], Zheng-Hong Huang [c,*], Lu-Ning Wang [a,d,*]

[a] School of Materials Science and Engineering, University of Science and Technology Beijing, Beijing 100083, China
[b] State Key Laboratory of Advanced Materials for Smart Sensing, General Research Institute for Non-Ferrous Metals, Beijing 101407, China
[c] Key Laboratory of Advanced Materials (MOE), School of Materials Science and Engineering, Tsinghua University, Beijing 100084, China
[d] State Key Laboratory for Advanced Metals and Materials, University of Science and Technology Beijing, Beijing 100083, China

ARTICLE INFO

Article history:
Received 16 October 2018
Received in revised form 26 November 2018
Accepted 9 December 2018
Available online 15 December 2018

Keywords:
Highly macroporous
g-C_3N_4
Nanohybrid
Interconnected network
Photocatalysis

ABSTRACT

It is of vital importance to construct highly interconnected, macroporous photocatalyst to improve its efficiency and applicability in solar energy conversion and environment remediation. Graphitic-like C_3N_4 (g-C_3N_4), as an analogy to two-dimensional (2D) graphene, is highly identified as a visible-light-responsive polymeric semiconductor. Moreover, the feasibility of g-C_3N_4 in making porous structures has been well established. However, the preparation of macroporous g-C_3N_4 with abundant porous networks and exposure surface, still constitutes a difficulty. To solve it, we report a first facile preparation of bimodal macroporous g-C_3N_4 hybrids with abundant in-plane holes, which is simply enabled by in-situ modification through thermally treating the mixture of thiourea and $SnCl_4$ (pore modifier) after rotary evaporation. For one hand, the formed in-plane macropores endow the g-C_3N_4 system with plentiful active sites and short, cross-plane diffusion channels that can greatly speed up mass transport and transfer. For another, the heterojunctions founded between g-C_3N_4 and SnO_2 consolidate the electron transfer reaction to greatly reduce the recombination probability. As a consequence, the resulted macroporous g-C_3N_4/SnO_2 nanohybrid had a high specific surface area (SSA) of 44.3 m^2/g that was quite comparable to most nano/mesoporous g-C_3N_4 reported. The interconnected porous network also rendered a highly intensified light absorption by strengthening the light penetration. Together with the improved mass transport and electron transfer, the macroporous g-C_3N_4/SnO_2 hybrid exhibited about 2.4-fold increment in the photoactivity compared with pure g-C_3N_4. Additionally, the recyclability of such hybrid could be guaranteed after eight successive uses.

1. Introduction

Photoenergy conversion offers a practical solution to the ever increasing energy and environmental issues [1–3]. Generally, the reactivity of a photoenergy conversion system depends heavily on its physicochemical and electrochemical structures, which can influence a series of photophysical events (i.e., photon absorption, exciton formation, charge transfer, and catalytic surface reactions) [4–11]. Steady progress is being made in developing new photoactive materials with tailored functions, particularly when visible light is used [12–17]. As the core of photocatalysis, charge transfer at the solid/water interface has been proven to dominate the electrochemical kinetics of the photoactive materials [18], and this rate-limiting charge transfer reaction is closely related to the surface concentrations of carriers and reactants. On this basis, increasing effort has been devoted to construct hierarchical porous nanostructures, which will undoubtedly endow the photoactive materials with better solar absorption and electron transfer abilities [19–21]. In detail, the effectiveness of the nano- and mesopores is strongly associated with the large accessible surface area, thereby offering more active sites or interfacial area for carrier generation and charge transfer [22–24]. While the advantage of macropores is that they can offset the transport limitations in pure nano- or mesopores, through facilitating the diffusion kinetics of reactants and products for significant mass transport [25,26]. In addition to the improved charge transfer reaction, an enhanced light harvesting capability can be ensured due to the multireflection within interconnected open networks. Among the studied por-

* Corresponding authors.
E-mail addresses: zhhuang@mail.tsinghua.edu.cn (Z.-H. Huang), luning.wang@ustb.edu.cn (L.-N. Wang).

https://doi.org/10.1016/j.scib.2018.12.015
2095-9273/

ous photocatalysts, nano/mesoporous systems have constituted the major part, but they are still deeply limited by the narrow pore sizes that are not effective for significant mass transport and access [27]. Making highly macroporous system seems a satisfactory solution of this aspect, especially when the issue on the significant loss of specific surface area (SSA) is well addressed. Therefore, a hierarchical porous system with well-developed macroporosity is highly sought after.

Carbon-based materials stand out as an exciting porous structure, and the pores can be produced and tuned during the carbonization of large molecules (e.g., polymers, biomolecules). Graphitic carbon nitride (g-C_3N_4), in particular, has emerged as a front runner because of its suitable bandgap (~2.7 eV), chemical stability, as well as the ease of making thin-layer nanosheets and porous structures [16,28–35]. So far, porous g-C_3N_4 has shown great photocatalytic capabilities in visible-light water splitting, CO_2 capture, disinfection and etc. [17,36–41]. The pores of mostly studied g-C_3N_4 arise from pyrolysis of carbon precursors, but with poor porosity. Further attempts have been carried out to employ hard or soft templates in yielding a variety of nano- and/or mesoporous g-C_3N_4 architectures. Table 1 gives a detailed comparison of the various porous g-C_3N_4 in the field of photocatalysis. The use of hard templates is appealing for synthesis of well-ordered or uniform pores, but usually adds an impediment as regards the costly functionalized templates and complex removal procedures. The soft templates, on the other hand, are apt to decompose completely upon elevated thermal treatment, but the extra carbon yield tends to weaken the reactivity by hiding some active sites of the catalysts. Apart from such cases, there are few examples on preparing porous g-C_3N_4 with high macroporosity, especially considering the beneficial effect of macropores in enhancing the mass transport/-transfer and light absorption [42]. Therefore, it is necessary to finger out a scalable solution to synthesize high-performance macroporous g-C_3N_4 system for efficient solar energy conversion.

In this context, we report a first facile synthesis of bimodal macroporous g-C_3N_4/SnO_2 nanohybrids with enhanced photocatalytic activity. It utilizes thiourea as the g-C_3N_4 precursor, $SnCl_4$ as the pore modifier (Fig. 1). A homogeneous mixture of thiourea and $SnCl_4$ was first prepared by rotatory evaporation of their aqueous solution, and then underwent thermal treatment at 550 °C in air. During this process, decomposition-polymerization of thiourea took place to give the formation of g-C_3N_4. As recognized, simple pyrolysis of thiourea is not likely to do a good job because of the poor porosity. Here, the involvement of $SnCl_4$ could encourage a great modification over the pristine g-C_3N_4 on account of its decomposition. According to some reported work, the hydrolysis product of $SnCl_4$ could be partly identified as hydrous SnO_2 and HCl. The release of gaseous HCl and more H_2O could act both as an etchant and a soft template to tune the pore formation. The co-product, SnO_2, was then coupled with g-C_3N_4 to render the formation of g-C_3N_4/SnO_2 hybrids. As a consequence, the obtained hybrids exhibited a high macroporosity with a pore volume of 2.638 cm^3/g, and SSA up to 44.3 m^2/g, a value comparative to that of nano/mesoporous g-C_3N_4 [43,45,49,51]. Taking advantage of the high macroporosity, g-C_3N_4/SnO_2 hybrids displayed effective light harvesting, large interfaces for fast charge transfer, as well as wide open networks for mass transport. Therefore, great enhancement of photoactivity was achieved by the obtained hybrids towards visible-light degradation of organic waste. Moreover, long-term stability could be guaranteed after several repeated runs. In view of these merits, the fabrication of macroporous photocatalysts with high SSA could form the basis of a stable and efficient photoconversion system.

2. Experimental

2.1. Preparation

$SnCl_4{\cdot}5H_2O$ and 10.8 g of thiourea were mixed in a mass ratio of 1:50, 1:40, 1:30, 1:20, and 1:20, respectively. The mixture was separately dissolved in 80 mL of deionized water under continuous stirring for 1 h. Subsequently, the solution was concentrated to dryness by rotatory evaporation at 60 °C. The dried mixture was then put into a crucible with a cover and calcined at 550 °C for 2 h in a muffle furnace, with a heating rate of 10 °C/min. The resulting yellow product was collected and ground into powders for further use. The corresponding product was denoted as Hybrid V, Hybrid IV, Hybrid III, Hybrid II, and Hybrid I, accordingly. Pure g-C_3N_4 and SnO_2 were also gotten by this method for comparison.

Table 1
Comparison of the reaction conditions and pore structures for the typical g-C_3N_4 samples.

Sample	Reaction precursor, temperature, time & atmosphere	Template requirement	Pore status	SSA (m^2/g)	Pore volume (cm^3/g)	Average pore size (nm)	Refs.
Bulk g-C_3N_4 (general condensation)	Varied	Free	Poor porosity	<10	–	–	
Bulk g-C_3N_4	Dicyandiamide, 560 °C, 2 h, N_2	PSB[a], removed with NH_4HF_2	Mesoporous	~37	~0.28	~36	[43]
Bulk g-C_3N_4	Melamine, 600 °C, 4 h, Ar	P123, self-dissolved	Mesoporous	~90	–	~15	[44]
g-C_3N_4/Ag_3PO_4	Urea, 550 °C, 4 h, air	No template	Mesoporous	~21	~0.083	~16	[45]
g-C_3N_4 tubes	Melamine, 600 °C, 4 h, air	SiO_2, removed with HF	Meso/macroporous	~107	–	One: ~10; the other:~50–90	[46]
Bulk g-C_3N_4 (enclosed condensation)	Urea, 550 °C, 4 h, Air	Free	Mesoporous	~141	~1.041	30–60	[47]
g-C_3N_4 ultrathin nanosheet	Melamine & glutaraldehyde, 800 °C, 2 h, Air	Cyanuric acid, self-dissolved	Mesoporous	~84	–	~3	[48]
Brookite/anatase TiO_2/g-C_3N_4	Hexadecylamine, 550 °C, 4 h, N_2	Free	Mesoporous	~37	~0.2	~18	[49]
g-C_3N_4/TiO_2	Melamine, 550 °C, 2 h, Air	Free	Meso/macroporous	~70	~0.193	One: ~10; the other:>50	[50]
TiO_2 trapped g-C_3N_4	Dicyandiamide, 560 °C, 2 h, N_2	PSB, removed with NH_4HF_2	Mesoporous	~63	~0.29	~20	[43]
g-C_3N_4 beads	Dicyandiamide, 530–600 °C, 2 h, N_2	PSB, removed with NH_4HF_2	Meso/macroporous	~58	~0.15	30–90	[51]
g-C_3N_4 nanosheet	Melamine, 550 °C, 4 h, air & 500 °C, 2 h, air	Free	Mesoporous	~190	~0.61	5–25	[52]

[a] PSB for porous SiO_2 beads.

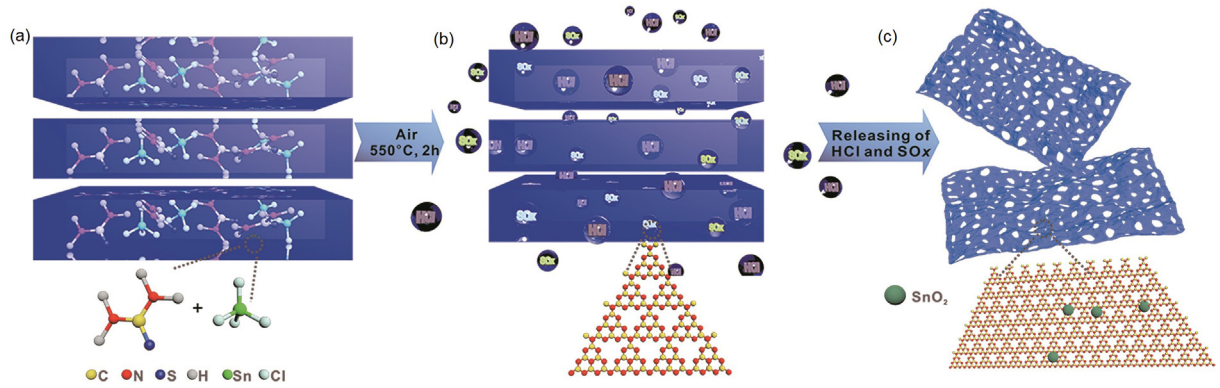

Fig. 1. (Color online) Schematic illustration of the facile design of the highly macroporous g-C_3N_4 system. (a) Homogeneous mixing of thiourea and $SnCl_4$ by rotatory evaporation. (b) Pyrolysis of thiourea modified by decomposition of $SnCl_4$. (c) Final production of the highly macroporous g-C_3N_4 system due to large amount of gas release.

2.2. Characterizations

The morphology was observed using scanning electron microscope (SEM, FEI Quanta 200), high resolution transmission electron microscope (HRTEM, JEM-2100F) equipped with an X-ray energy-dispersive spectrometer (EDS, Oxford EDS X-MaxN80T). Thermogravimetric (TG) analysis was carried on TA-SDTQ600 thermal analyzer. The X-ray diffraction (XRD) patterns were recorded on the Ultima IV X-ray diffractometer with Cu Kα radiation. The Fourier transform infrared spectroscopy (FTIR) of these samples was recorded on Excalibur 3100 IR spectrometer using a KBr pellet technique. The Raman spectra were measured at a dispersive Raman spectrometer in Via-Reflex. The X-ray photoelectron spectroscopy (XPS) measurement was performed by a monochromatic Al Kα X-ray radiation (1,486.6 eV). The porous structure was investigated by nitrogen-adsorption– desorption (QUADRASORB Si). UV–Vis absorption spectra were recorded with Cary 5000 Varian spectrophotometer. Photoluminescence (PL) of the samples measurements were run on an F-4500 fluorescence spectrophotometer with an excitation wavelength of 365 nm. Photocurrent measurements were conducted in a conventional three-electrode cell system by using a CHI660E electrochemical station. The cleaned indium tin oxide (ITO) glass deposited with samples, a Pt mesh, and a saturated calomel electrode (SCE) were respectively used as working electrodes, counter electrode, and reference electrode. A 0.1 mol/L Na_2SO_4 was used as the electrolyte (pH 6.84). The photoelectrode was illuminated with AM 1.5G simulated sunlight (100 mW/cm^2). The total organic carbon (TOC) concentration was measured using TOC analyzer (TOC-VCPH, Shimadzu).

2.3. Photoactivity evaluation

2.3.1. Physical adsorption

A 5 mg of the as-prepared sample was dispersed in methylene blue (MB, 0.01 mmol/L, 50 mL) aqueous solution in the dark overnight to obtain an adsorption–desorption equilibrium, and then one aliquot was withdrawn and tested by UV–Vis spectrophotometer.

2.3.2. Photocatalytic performance

After the adsorption–desorption equilibrium, the as-prepared sample was collected and dispersed in a new fresh solution of MB (0.01 mmol/L, 50 mL) again. The solution was illuminated with AM 1.5G simulated sunlight (100 mW/cm^2). At a given time interval of irradiation, small aliquots were withdrawn and measured by UV–Vis spectrophotometer.

3. Results and discussion

The morphology and macrostructure of the as-prepared samples were investigated in SEM (Fig. 2) and TEM (Fig. 3) images. In contrast to the dense stacking structure of bulk g-C_3N_4 (Figs. 2a and 3a) by direct polycondensation of thiourea, the hybrids were comprised of loose and small aggregates with many pores (Figs. 2b–f and 3b–f). Notably, the structure of Hybrid II (Fig. 2b) appeared to be more loose and porous than that of others, and a large number of in-plane holes could even be clearly observed in the HRTEM image with the diameter of 50–200 nm (Fig. 3b). A selected area electron diffraction (SAED) pattern revealed the polycrystalline nature of g-C_3N_4 (inset, Fig. 3a–f). Pure g-C_3N_4 displayed two distinct diffraction rings indexed to the (1 0 0) and (0 0 2) planes, respectively (inset, Fig. 3a) [20,51]. Such clear and sharp rings could also be found in the less-doped Hybrid V (inset, Fig. 3b). But as more $SnCl_4$ was added, the polycrystalline diffraction rings became increasingly blurred and vague, until the very vague rings were seen in Hybrid I (Fig. 3f). The unclear diffraction rings suggested a weakened crystallization in the hybrids, and the reason was further explored by TG analysis. As shown in Fig. S1 (online), the initial weight loss temperature of the hybrids was lower than that of pure g-C_3N_4, and gradually declined from Hybrid V to I. The weaker thermal stability of the hybrids suggested that the introduction of precursor $SnCl_4$ caused weakened cross-linked rings of g-C_3N_4, and increased its oxidation degree [53], which thereby explained the loss of crystallization.

The HRTEM images of representative Hybrid II (Fig. 3g and h) further confirmed the polycrystallinity of g-C_3N_4, as well as the presence of high crystalline SnO_2. In Fig. 3h, the locally magnified image of SnO_2 nanoparticles revealed the lattice fringes with basal distances of 2.64 Å, corresponding to the (1 1 0) lattice spacing of tetragonal SnO_2. Moreover, the scanning transmission electron microscopy (STEM) image and the corresponding elemental mapping (Fig. S2 online), clearly indicated the expected homogeneous spatial distribution of SnO_2 over g-C_3N_4 network. Herein, proper addition of $SnCl_4$ in the precursors would lead to a modification over the pore structure of the obtained g-C_3N_4, and the modified structure provides a logical opportunity to improve the photochemical and photophysical behaviors inside it by enlarging the transfer/transport pathways as well as accessible sites.

The structure was further examined by a combined analysis of XRD and FTIR. In Fig. 4a, the XRD patterns of pure g-C_3N_4 featured two pronounced diffraction peaks at 12.8° and 27.5°, which could be assigned to the (0 0 2) and (1 0 0) plane, respectively [54]. It is well acknowledged that g-C_3N_4 is constructed via tri-s-triazine units. As depicted in Fig. 4a, the minor (1 0 0) peak corresponds to the in-plane repeated tri-striazine units, while the main peak

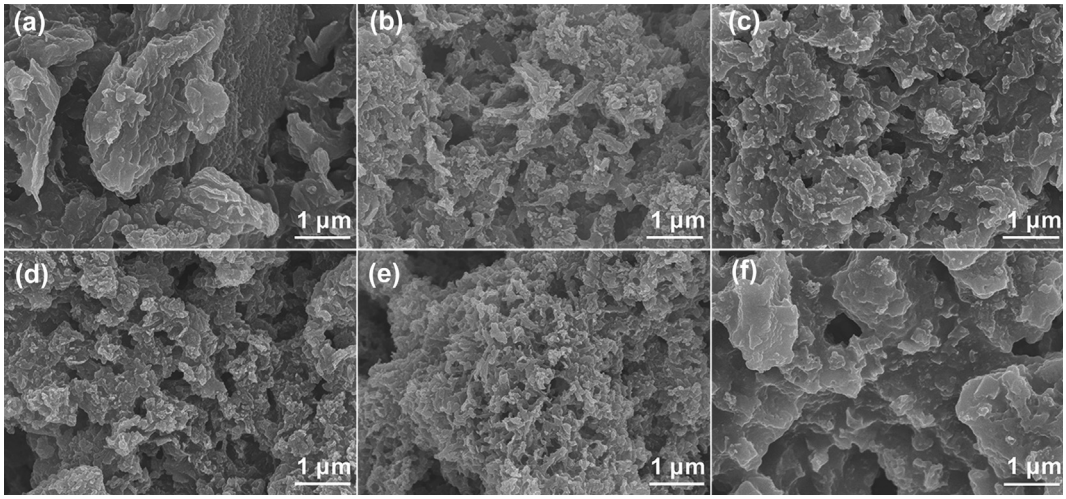

Fig. 2. SEM images of pure g-C_3N_4 (a), Hybrid V (b), Hybrid IV (c), Hybrid III (d), Hybrid II (e), and Hybrid I (f).

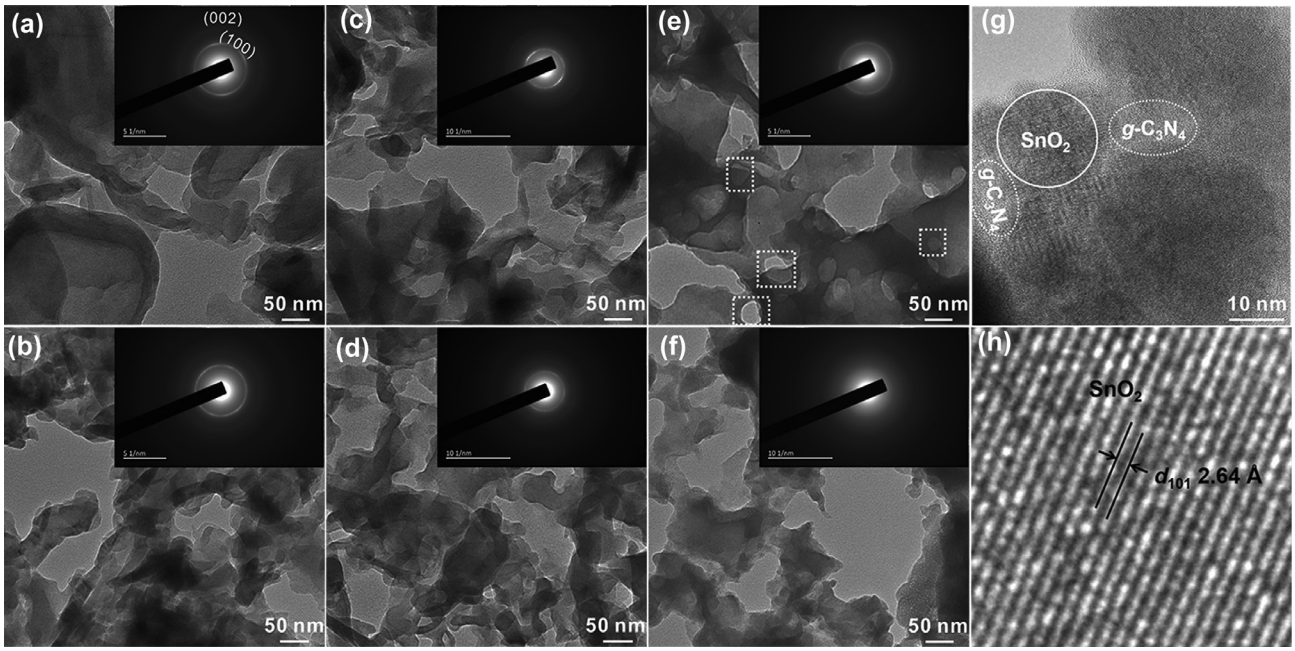

Fig. 3. TEM images of pure g-C_3N_4 (a), Hybrid V (b), Hybrid IV (c), Hybrid III (d), Hybrid II (e), and Hybrid I (f). Insets are their corresponding SAED patterns; (g, h) HRTEM images of the SnO_2 and g-C_3N_4 nanograins in Hybrid II.

(0 0 2) is relevant to the interlayer stacking of the conjugated aromatic segments [47]. Compared with pure g-C_3N_4, the (1 0 0) diffraction peak totally disappeared in the hybrids, while the intensity of (0 0 2) peak showed a gradual decrease until it was significantly weakened in Hybrid I. This result indicated that the involvement of precursor $SnCl_4$ would partially destroy the graphitic structure, and cause some alteration either to interlayer stacking or to interplanar structural packing [55]. The reduced crystallization also agrees well with the TEM observation. Besides, the (0 0 2) peak was somewhat broadened in the hybrids, which was a sign of the confined growth of the g-C_3N_4 matrix under the rich gaseous atmosphere. On the other hand, no obvious diffraction peaks featuring SnO_2 were detected in the hybrids, possibly because of the very small amount of it.

Fig. 4b showed a comparison of the FTIR spectra of the as-prepared samples. In the case of pure g-C_3N_4, the dominant bands in the 1,200–1,650 cm^{-1} region stemmed from the stretching modes of the aromatic C—N heterocycles. The sharp peak at 810 cm^{-1} revealed the formation of heptazine rings as the building unit of the g-C_3N_4 network. In addition, the stretching vibrations of O—H and N—H groups covered a broad region around 2,700–3,500 cm^{-1}, which were mainly ascribed to the surface N—H residues and absorbed H_2O [56]. For pure SnO_2 (Fig. S3 online), there were two characteristic peaks of Sn—O at about 530 cm^{-1} (Sn—OH bond stretching) and 640 cm^{-1} (the vibration of Sn—O—Sn bonds) [57,58]. As for the hybrids, the peaks typical of g-C_3N_4 were mostly observed, but those featuring SnO_2 were too weak to be clearly detected.

XPS measurement is a useful tool to investigate the chemical states and the chemical composition of the hybrids. Fig. S4a (online) compared the XPS survey spectrum for the pure g-C_3N_4 and the representative Hybrid I. As expected, the aforementioned Hybrid I was mainly composed of C, N, Sn, and O elements, on contrary to the only presence of C, and N elements (with negligible O)

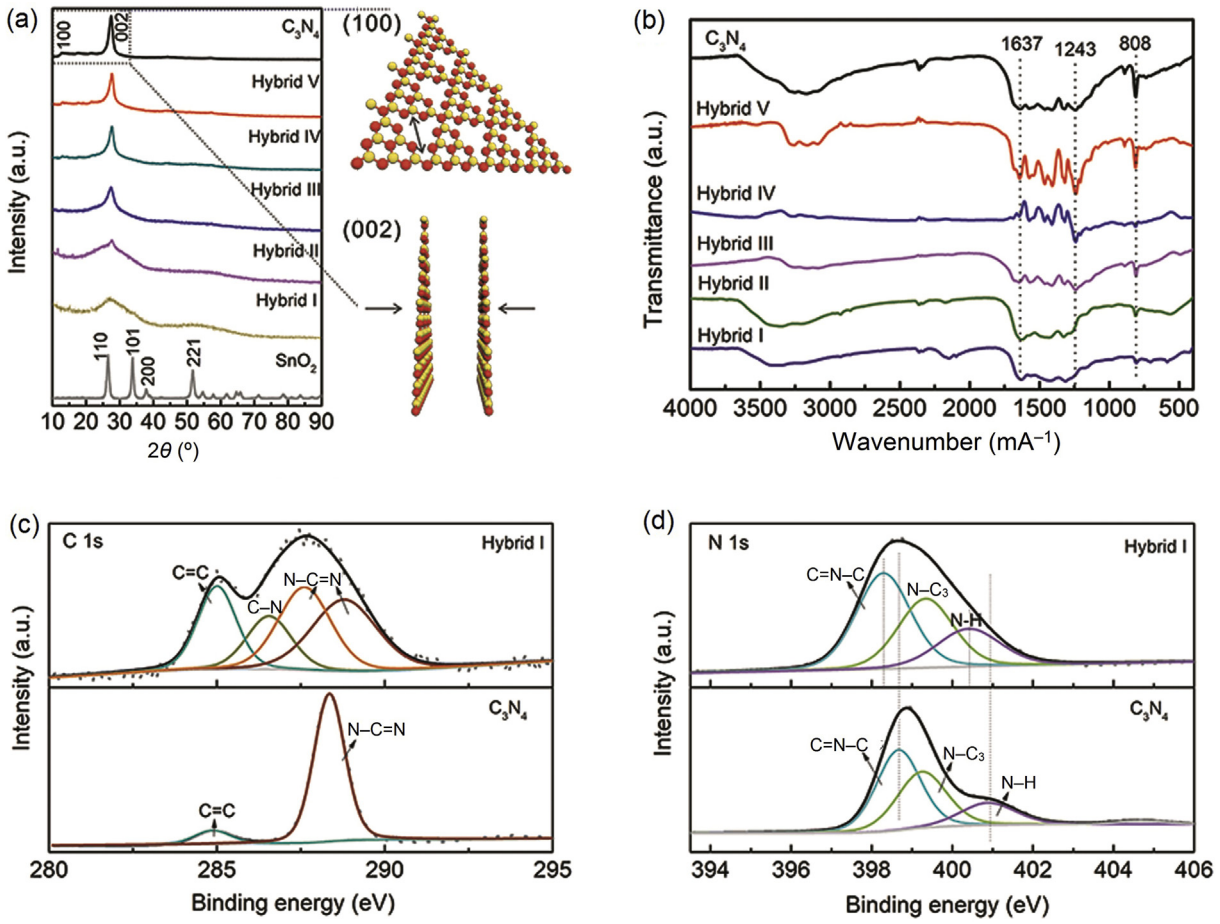

Fig. 4. (Color online) XRD (a), IR (b), C 1s (c) and N 1s (d) XPS spectra of the as-prepared samples.

in pure *g*-C_3N_4. The trace amount of O most likely originated from adsorbed H_2O molecules. The high-resolution C 1s and N 1s XPS spectra for the obtained *g*-C_3N_4 and Hybrid I were presented in Fig. 4c and d. The C 1s spectrum for *g*-C_3N_4 consisted of two features of binding energy values positioned at 284.8 and 288.3 eV (Fig. 4c) [59,60]. The minor peak at 284.8 eV was typically assigned to the sp^2 C=C bonds. The main contribution peak whose maxima were situated at 288.3 eV, corresponded to N=C—N coordination in the *s*-triazine aromatic ring attached to NH_2 group. By comparison, Hybrid I exhibited a broader feature in the C 1s peak that was fitted with four components. The peaks at 284.9 and 286.5 eV were attributed to the C=C, C—N coordination between aromatic rings, and the two peaks at 287.6 and 288.8 eV could be identified as N=C—N coordination. The deconvolution of C 1s peak from two to five peaks with binding energies at approximately 284.6, 285.9, 287.7 and 288.2 eV, has been mentioned in previous reports, but the relative changes among these different components at different percentage of nitrogen are not clearly understood yet [61–63]. While in the N 1s spectra (Fig. 4d), the N 1s peak of *g*-C_3N_4 was decomposed into three components at 398.7, 399.3, and 400.9 eV, corresponding to sp^2-hybridized nitrogen (C=N—C, edge N atoms), tertiary nitrogen (N—$(C)_3$, inner and bridge N atoms) and amino functional groups (C=N—H) caused by incomplete condensation, respectively (Fig. 5a) [47]. Similar results were also noticed with Hybrid I, but it was notable that the N 1s peak of Hybrid I moved to a lower binding energy (C=N—C at 398.3 eV, and C=N—H at 400.5 eV) when compared with that of pure *g*-C_3N_4. This suggested an interfacial interaction across the components in the hybrids.

Here, the presence of SnO_2 in the hybrids was further confirmed by the high-resolution Sn 3d and O 1s spectra. In the Sn 3d spectra for SnO_2 and the hybrids (Fig. S4b online), two symmetrical peaks at 486.6 and 494.9 eV were attributed to Sn $3d_{5/2}$ and Sn $3d_{3/2}$, respectively [64]. This was in fairly good accordance with the energy splitting reported for SnO_2 [65]. In line with Sn 3d spectra, the O 1s spectra (Fig. S3c online) showed a XPS peak at approximately 530.4 eV for both SnO_2 and the hybrids, which corresponded to the oxygen species in the reported SnO_2. Moreover, a slight upward shift of the peak was displayed by the hybrids compared with pure SnO_2, which was another evidence of the interfacial interaction between the *g*-C_3N_4 and SnO_2 [66].

The Raman spectra were also investigated to confirm the presence of SnO_2 in the hybrids. As displayed in Fig. 5b, pure *g*-C_3N_4 exhibited several typical peaks at about 708, 978 (the triazine skeletal vibration), and 1,234 cm^{-1} [67]. While for pure SnO_2 (Fig. S5 online), the spectrum was characterized by the presence of three peaks located at 476, 631 and 771 cm^{-1}, indexed to E_g, A_{1g} and B_{2g} vibration modes, respectively [68]. Note that the Raman bands for the hybrids contained the respective peaks of both *g*-C_3N_4 and SnO_2, which confirmed the coexistence of *g*-C_3N_4 and SnO_2 in the hybrids.

The pore structures and the Brunauer-Emmett-Teller (BET) surface area of the as-prepared samples were measured by N_2 adsorption-desorption measurements at 77 K. As expected, the hybrids possessed a much larger BET SSA than that of pure *g*-C_3N_4 (Fig. 5c). In detail, the SSA values increased in the following order: *g*-C_3N_4 < Hybrid I < Hybrid V < Hybrid IV < Hybrid III < Hybrid II. Particularly, the SSA of Hybrid II was determined to be

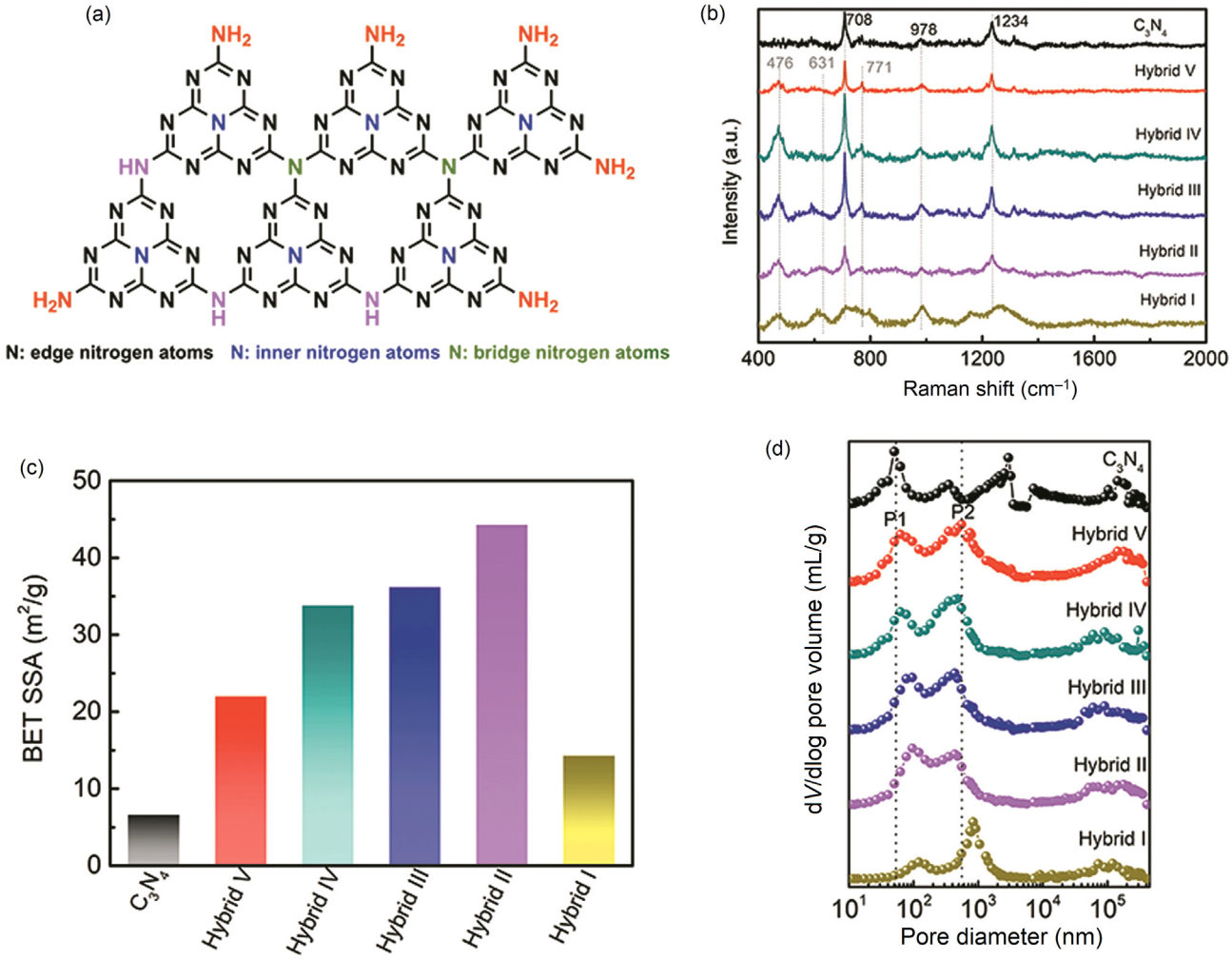

Fig. 5. (Color online) Physicochemical characterizations of the as-prepared samples. (a) Supercell modal of monolayer g-C_3N_4 in a segment with SiC heptazine units. Raman spectra (b), the BET SSA (c), and PSD (d) of the as-prepared samples.

44.3 m^2/g, which was 6.5 times higher than that of g-C_3N_4. Fig. 5d displayed the pore size distribution (PSD) curves of the samples. We could see that g-C_3N_4 had a quite broad distribution of macropores with size ranging from tens of nanometers to several thousand nanometers, and no significant presence of mesopores or micropores was observed. Such macroporous structure might originate from the random interstitial holes caused by aggregates of massive g-C_3N_4 particles [69]. By comparison, the PSD was largely narrowed down, and became distinctly bimodal for the hybrids with the two peaks denoted as P1 and P2. The total pore volume of Hybrid II here was determined to be ~2.638 cm^3/g, a value much higher than the 0.875 cm^3/g for g-C_3N_4. Note that this value together with the SSA was quite exciting for the macroporous g-C_3N_4, which was comparable to those realized by templating methods.

It should also be pointed out that the extremely high pore volume of Hybrid II might be derived from a large number of in-plane holes and loose aggregation of g-C_3N_4 layers. As proposed in Fig. 1, the additional precursor $SnCl_4$ played an important role in the formation of the highly macroporous g-C_3N_4. The plenty of bubbles released from the decomposed $SnCl_4$ would act as an etchant and soft template, which were able to penetrate the g-C_3N_4 network to minimize the agglomeration and also helped to produce the 3D interconnected porous structures. Hence, the reduced agglomeration led to the disappearance of the quite large holes with the size of 700–4,000 nm in pure g-C_3N_4, and gave rise to the bimodal P1 and P2. Furthermore, with increased bubble etching from Hybrid V to II, the small holes (P1) were expanded, and large ones (P2) were downsized. Thereby the PSD became narrow to give elevated SSA. We could also clearly see that the pore size of P1 (Hybrid II, Fig. 5d) was quite consistent with the in-plane holes in TEM observation (Fig. 3b). It was apparent that Hybrid II possessed a much narrow PSD, which well explained its highest SSA. However, when overdose of precursor $SnCl_4$ was added, the excessive bubble release would result in quite expanded holes (for both P1 and P2) as in Hybrid I, and greatly reduced its SSA. More detailed comparisons on the BET surface area and PSD were presented in Table 2. Here, the resulted high accessible surface area and interconnected pore openings were bound to promote the kinetics of photocatalytic reaction by enlarging the accessibility of diffusing species as well as facilitating mass transfer and transport.

The highly macroporous structure is thought to exert a great effect on the UV–Vis absorption of the as-prepared hybrids. In Fig. 6a, it was found that the absorption intensity showed a gradual increase with increasing the SnO_2 content in hybrids, and the strongest seen with Hybrid II. Meanwhile, a remarkable red shift of the absorption edge was observed in Hybrid I (410 nm) compared with pure g-C_3N_4 (386 nm). The increased intensity indicated that the continuous macropore channels would be in great

Table 2
Physical and structural properties of the macroporous samples.

Sample	SSA (m^2/g)	Pore size (nm)	Total volume (cm^3/g)	Adsorption of MB (%)
g-C_3N_4	6.662	P1: 50 P2: 350 The other: 700–4,000	0.875	20.3
Hybrid V	22.024	P1: 60 P2: 580	1.275	36.2
Hybrid IV	33.851	P1: 60 P2: 480	1.732	39.2
Hybrid III	36.238	P1: 90 P2: 400	1.736	47.5
Hybrid II	44.342	P1: 100 P2: 430	2.638	72
Hybrid I	14.336	P1: 110 P2: 800	1.062	25.7

favor of light penetration into the solid samples and that larger volume of moderate macropores led to deeper optical penetration. For Hybrid I, the extended absorbance was considered to arise from an enhanced electron delocalization through charge transfer to reduce the band energy. Thereby, the intensified light absorption in the hybrids could possibly provide more photocharges needed for the photocatalytic reactions.

The photocatalytic performance of the prepared samples was evaluated in degrading MB under simulated sunlight irradiation (100 mW/cm^2). Ahead of that, the adsorption properties of MB onto the surface of the different samples were tested, as it is an important step in photocatalytic degradation [70]. After adsorption-desorption equilibrium in the dark overnight, the remaining concentration fractions of MB were gotten from UV–Vis absorption measurements (Fig. S6 online). Table 2 also listed the adsorption changes in detail. As it showed, only 21.6% was adsorbed by pure g-C_3N_4, whereas a large amount of MB up to 66.6% was adsorbed on the framework of Hybrid II. The result coincided well with the SSA changes. When it came to the photocatalytic efficiency (Fig. 6b), it was found that negligible degradation took place during the dark, and during light on, MB remained almost stable in the absence of any catalyst. Under the action of the as-prepared samples, the photoreactivity (C/C_0) followed an order of SnO_2 (26%) < g-C_3N_4 (35%) < Hybrid I (53%) < Hybrid V (59%) < Hybrid IV (65%) < Hybrid III (71%) < Hybrid II (85%). To investigate the mineralization degree of MB in the photocatalytic reaction, the concentration of TOC under the action of Hybrid II was measured, as shown in Fig. 6c. It can be seen that after 100 min reaction the TOC were removed almost by 98%, from the initial 4.85–0.09 mg/L. An analogous conclusion could be made on the improved photoreactivity, which emphasized the importance of increased macropores. The high macroporosity could not only provide sufficient light penetration and surface reactive sites, but enabled efficient electron transfer pathway and fast mass transport through the short diffusion/transfer distance due to the interconnected network. In addition, charge separation across the abundant g-C_3N_4/SnO_2 interfaces also contributed greatly.

Photoluminescence (PL) intensity, representative of radiative charge recombination, was applied as an indirect evidence to investigate the charge separation. It could be clearly seen from Fig. 7a that the PL emission of all the hybrids was quenched greatly compared with that of pure g-C_3N_4, revealing that the probability of photocarrier recombination was largely inhibited. Moreover, an upward trend was witnessed in the inhibition degree as the SnO_2 content increased in the hybrids. The ~90% PL quenching in the hybrids clearly implied the photoinduced electron transfer process across the interface [71,72], and also the larger contacted area between g-C_3N_4 and SnO_2 offered higher efficiency of the electron transfer. The significant reduction in Hybrid I indicated the strongest electron transfer between g-C_3N_4 and SnO_2 moieties due to the increased amount of SnO_2 moiety, and this result necessarily explained the largely extended absorption with Hybrid I as Fig. 6a showed. Similar result could also be found in photocurrent response tests under chopped illumination (100 mW/cm^2) in Fig. 7b. The remarkably enhanced photocurrent generation of Hybrid II could be attributed to the large number of in-plane macropores, which greatly facilitated the mass transfer and improved the charge separation efficiency. Herein, the enhanced light absorption along with the reduced recombination rate promise to afford the hybrids with improved photocatalytic activity.

Scavenger tests were performed to quench the reactions, hence to evaluate the contribution of the oxidative species to photodegradation. The results (Fig. 7c) showed that the addition of *tert*-butyl alcohol (TBA), ·OH scavenger, reduced the reactivity by ~42%, while the addition of superoxide dismutase (SOD), $O_2^{\cdot-}$ scavenger, reduced the reactivity by ~37%. It is highly recognized that

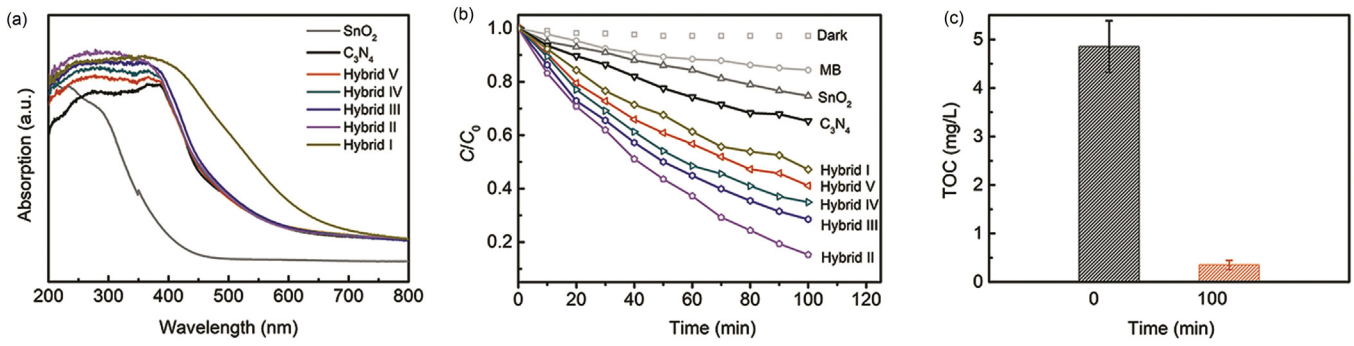

Fig. 6. (Color online) UV–Vis absorption spectra (a) and photocatalytic degradation (b) of MB using the as-prepared samples under solar light. (c) TOC concentration changed under the action of Hybrid II after 100 min of solar light irradiation. Solar light intensity in all measurements is 100 mW/cm^2.

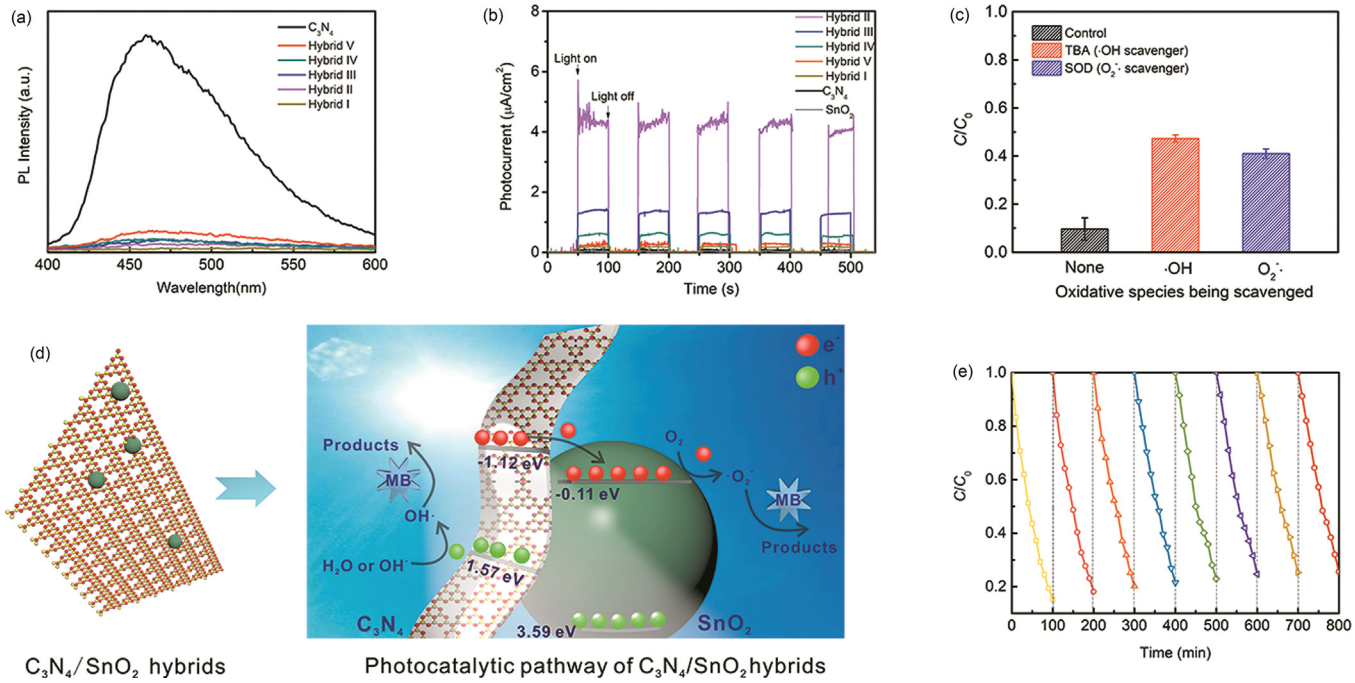

Fig. 7. (Color online) PL emission spectra (a), and photocurrent vs. time plots (b) at 1.23 V (vs. RHE) under chopped illumination (100 mW/cm^2). (c) The reactivity inhibition of MB degradation in the presence of scavengers (10 mmol/L of TBA as ·OH scavenger, 10 mmol/L of SOD as a O_2^-· scavenger). (d) Schematic illustrating the photocatalytic pathway of *g*-C_3N_4/SnO_2 hybrid. (e) Recycling experiment using Hybrid II for MB degradation under solar light (100 mW/cm^2).

both *g*-C_3N_4 and SnO_2 are active and stable semiconductors. SnO_2 has a lower-lying conduction band (CB) energy (E_{CB} = −0.11 eV) and valence band (VB) energy (E_{VB} = 3.59 eV) than *g*-C_3N_4 (E_{CB} = −1.12 eV, E_{VB} = 1.57 eV) [73]. For one hand, the well-matched band structures between *g*-C_3N_4 and SnO_2 allow a good combination of them for increased photoinduced electro transfer. For another, because of the high SSA, the large electron donor-electron acceptor interface provides a strong driving force to separate the spatial charges. For these reasons, the recombination probability of the charge carriers could be greatly inhibited, affording the formation of more active species for MB oxidation. Fig. 7d illustrated the electron transfer reaction in the MB medium. SnO_2 could absorb a small fraction of sunlight to generate active charge carriers, while major photon adsorption took place in *g*-C_3N_4 side, leading to the production of photogenerated charge carriers and diffusion of the carriers to the *g*-C_3N_4/SnO_2 interface. The generated electrons were injected from the CB of *g*-C_3N_4 into the CB of SnO_2 according to the potential established across the hybrid. The electrons could undergo reaction with molecular oxygen to form superoxide radical anion O_2^-·, in addition to minor reaction with H^+ to give hydroxyl radicals **.**OH. The holes left at *g*-C_3N_4 side could react with water, resulting in the generation of hydroxyl radical **.**OH. The resultant O_2^-· and **.**OH then participated in electron transfer reaction with MB to give its oxidized form. The products were then transported away to the medium.

To assess the practicability, the recycling experiment was performed on Hybrid II for MB degradation under solar light (Fig. 7e). The photocatalytic degradation underwent 100 min in each run, and eight repeated runs were conducted. After each run, a new fresh solution of MB was supplied to maintain its initial concentration. A slight decline in reaction rate was observed to confirm its reliability. After 8 successive cycles, almost 90% of its initial reactivity was guaranteed. The demonstrated stability implies that the as-prepared highly macroporous hybrid can work as an efficient photocatalyst for wastewater treatment, or environmental purification.

4. Conclusion

In summary, highly macroporous *g*-C_3N_4/SnO_2 hybrids were facilely prepared by heating the homogeneous mixture of thiourea and $SnCl_4$ after rotatory evaporation. The $SnCl_4$ was involved not only to modify the pore structure of *g*-C_3N_4 into nanosheets with abundant in-plane macropores, but also to produce SnO_2 in coupling with *g*-C_3N_4 to create charge transfer interfaces. Meanwhile, the intrinsic pore structure could simply be adjusted by changing the mass ratio of the precursors. As a result of the moderate in-plane macropores and active sites, the obtained *g*-C_3N_4/SnO_2 hybrids exhibited an intensified light absorption, and a remarkably increased separation efficiency of photogenerated electrons and holes. An optimization of the macropore structures gave rise to an improved SSA of 44.3 m^2/g comparable to most nano/mesoporous *g*-C_3N_4 reported. Compared with pure *g*-C_3N_4, the *g*-C_3N_4/SnO_2 hybrid exhibited 2.4 times higher photocatalytic activity for photooxidation of organic waste, and was proved to be an efficient and sustainable photocatalyst for repeated use. In view of the convenience and efficiency, the as-prepared macroporous system promises to be applied for practical environment treatment.

Conflict of interest

The authors declare that they have no conflict of interest.

Acknowledgments

This work was supported by the National Key Research and Development Program of China (2016YFB0700300), the National Natural Science Foundation of China (51503014, 51501008) and the State Key Laboratory for Advanced Metals and Materials (2016Z-03).

Appendix A. Supplementary data

Supplementary data to this article can be found online at https://doi.org/10.1016/j.scib.2018.12.015.

References

[1] Chu S, Majumdar A. Opportunities and challenges for a sustainable energy future. Nature 2012;488:294–303.
[2] Chowdhury FA, Trudeau ML, Guo H, et al. A photochemical diode artificial photosynthesis system for unassisted high efficiency overall pure water splitting. Nat Commun 2018;9:1707–15.
[3] Detz RJ, Reek JNH, Van der Zwaan BCC. The future of solar fuels: when could they become competitive? Energy Environ Sci 2018;11:1653–69.
[4] Leow WR, Ng WKH, Peng T, et al. Al_2O_3 surface complexation for photocatalytic organic transformations. J Am Chem Soc 2016;139:269–76.
[5] Zhang Y, Wu B, Tang Y, et al. Prolonged electron lifetime in ordered TiO_2 mesophyll cell-like microspheres for efficient photocatalytic water reduction and oxidation. Small 2016;12:2291–9.
[6] Wang X, Liow C, Bisht A, et al. Engineering interfacial photo-induced charge transfer based on nanobamboo array architecture for efficient solar-to-chemical energy conversion. Adv Mater 2015;27:2207–14.
[7] Wang X, Liow C, Qi D, et al. Programmable photo-electrochemical hydrogen evolution based on multi-segmented CdS-Au nanorod arrays. Adv Mater 2014;26:3506–12.
[8] Yang C, Wang B, Zhang L, et al. Synthesis of layered carbonitrides from biotic molecules for photoredox transformations. Angew Chem Int Ed 2017;56:6627–31.
[9] Xu J, Luo L, Xiao G, et al. Layered $C_3N_3S_3$ polymer/graphene hybrids as metal-free catalysts for selective photocatalytic oxidation of benzylic alcohols under visible Light. ACS Catal 2014;4:3302–6.
[10] Long J, Chang H, Gu Q, et al. Gold-plasmon enhanced solar-to-hydrogen conversion on the 001 facets of anatase TiO_2 nanosheets. Energy Environ Sci 2014;7:973–7.
[11] Xu J, Chen Z, Zhang H, et al. $Cd_3(C_3N_3S_3)_2$ coordination polymer/graphene nanoarchitectures for enhanced photocatalytic H_2O_2 production under visible light. Sci Bull 2017;62:610–8.
[12] Huang D, Yan X, Yan M, et al. Graphitic carbon nitride-based heterojunction photoactive nanocomposites: applications and mechanism insight. ACS Appl Mater Interfaces 2018;10:21035–55.
[13] Makaremi M, Grixti S, Buter KT, et al. Band engineering of carbon nitride monolayers by N-type, P-type, and isoelectronic doping for photocatalytic applications. ACS Appl Mater Interfaces 2018;10:11143–51.
[14] Elbanna O, Fujitsuka M, Majima T. g-C_3N_4/TiO_2 mesocrystals composite for H_2 evolution under visible-light irradiation and its charge carrier dynamics. ACS Appl Mater Interfaces 2017;9:34844–54.
[15] Yu H, Shi R, Zhao Y, et al. Alkali-assisted synthesis of nitrogen deficient graphitic carbon nitride with tunable band structures for efficient visible-light-driven hydrogen evolution. Adv Mater 2017;29:1605148.
[16] Fu J, Yu J, Jiang C, et al. g-C_3N_4-based heterostructured photocatalysts. Adv Energy Mater 2018;8:1701503.
[17] Zhou C, Shi R, Shang L, et al. Template-free large-scale synthesis of g-C_3N_4 microtubes for enhanced visible light-driven photocatalytic H_2 production. Nano Res 2018;11:3462–8.
[18] He Y, Pang X, Jiang B, et al. Unconventional route to uniform hollow semiconducting nanoparticles with tailorable dimensions, compositions, surface chemistry, and near-infrared absorption. Angew Chem 2017;129:13126–31.
[19] Di T, Zhang J, Cheng B, et al. Hierarchically nanostructured porous TiO_2 (B) with superior photocatalytic CO_2 reduction activity. Sci China Chem 2018;61:344–50.
[20] Liang Q, Li Z, Huang ZH, et al. Holey graphitic carbon nitride nanosheets with carbon vacancies for highly improved photocatalytic hydrogen production. Adv Funct Mater 2015;25:6885–92.
[21] Zhao D, Gao Y, Nie S, et al. Self-assembly of honeycomb-like calcium-aluminum-silicate-hydrate (C-A-S-H) on ceramsite sand and its application in photocatalysis. Chem Eng J 2018;344:583–93.
[22] Liu B, Yang J, Zhao X, et al. The role of electron interfacial transfer in mesoporous nano-TiO_2 photocatalysis: a combined study of in situ photoconductivity and numerical kinetic simulation. Phys Chem Chem Phys 2017;19:8866–73.
[23] Liu C, Huang H, Ye L, et al. Intermediate-mediated strategy to horn-like hollow mesoporous ultrathin g-C_3N_4 tube with spatial anisotropic charge separation for superior photocatalytic H_2 evolution. Nano Energy 2017;41:738–48.
[24] Gan Y, Wei Y, Xiong J, et al. Impact of post-processing modes of precursor on adsorption and photocatalytic capability of mesoporous TiO_2 nanocrystallite aggregates towards ciprofloxacin removal. Chem Eng J 2018;349:1–16.
[25] Liang Q, Li Z, Yu X, et al. Macroscopic 3D porous graphitic carbon nitride monolith for enhanced photocatalytic hydrogen evolution. Adv Mater 2015;27:4634–9.
[26] Wei Y, Jiao J, Zhao Z, et al. 3D ordered macroporous TiO_2-supported Pt@CdS core-shell nanoparticles: design, synthesis and efficient photocatalytic conversion of CO_2 with water to methane. J Mater Chem A 2015;3:11074–85.
[27] Li B, Zhao J, Liu J, et al. Bio-templated synthesis of hierarchically ordered macro-mesoporous anatase titanium dioxide flakes with high photocatalytic activity. RSC Adv 2015;5:15572–8.
[28] Ye P, Liu X, Iocozzia J, et al. A highly stable non-noble metal Ni_2P co-catalyst for increased H_2 generation by g-C_3N_4 under visible light irradiation. J Mater Chem A 2017;5:8493–8.
[29] Guo Y, Li J, Yuan Y, et al. A rapid microwave-assisted thermolysis route to highly crystalline carbon nitrides for efficient hydrogen generation. Angew Chem Int Ed 2016;55:14693–7.
[30] Du A, Sanvito S, Li Z, et al. Hybrid graphene and graphitic carbon nitride nanocomposite: gap opening, electron-hole puddle, interfacial charge transfer, and enhanced visible light response. J Am Chem Soc 2012;134:4393–7.
[31] Xu Q, Cheng B, Yu J, et al. Making co-condensed amorphous carbon/g-C_3N_4 composites with improved visible-light photocatalytic H_2-production performance using Pt as cocatalyst. Carbon 2017;118:241–9.
[32] Yu Y, Wang C, Luo L, et al. An environment-friendly route to synthesize pyramid-like g-C_3N_4 arrays for efficient degradation of rhodamine B under visible-light irradiation. Chem Eng J 2018;334:1869–77.
[33] Jourshabani M, Shariatinia Z, Badiei A. High efficiency visible-light-driven Fe_2O_3-xS_x/S-doped g-C_3N_4 heterojunction photocatalysts: direct Z-scheme mechanism. J Mater Sci Technol 2018;34:1511–25.
[34] Mousavi M, Habibi-Yangjeh A, Seifzadeh D. Novel ternary g-C_3N_4/Fe_3O_4/$MnWO_4$ nanocomposites: synthesis, characterization, and visible-light photocatalytic performance for environmental purposes. J Mater Sci Technol 2018;34:1638–51.
[35] Yan Q, Huang GF, Li DF, et al. Facile synthesis and superior photocatalytic and electrocatalytic performances of porous B-doped g-C_3N_4 nanosheets. J Mater Sci Technol 2018;34:2515–20.
[36] Fu J, Bie C, Cheng B, et al. Hollow CoS_x polyhedrons act as high-efficiency cocatalyst for enhancing the photocatalytic hydrogen generation of g-C_3N_4. ACS Sustain Chem Eng 2018;6:2767–79.
[37] Fu J, Zhu B, Jiang C, et al. Hierarchical porous O-doped g-C_3N_4 with enhanced photocatalytic CO_2 reduction activity. Small 2017;13:1603938.
[38] Tian N, Zhang Y, Li X, et al. Precursor-reforming protocol to 3D mesoporous g-C_3N_4 established by ultrathin self-doped nanosheets for superior hydrogen evolution. Nano Energy 2017;38:72–81.
[39] Jo WK, Selvam NCS. Z-scheme CdS/g-C_3N_4 composites with RGO as an electron mediator for efficient photocatalytic H_2 production and pollutant degradation. Chem Eng J 2017;317:913–24.
[40] Li X, Zhu W, Lu X, et al. Integrated nanostructures of CeO_2/attapulgite/g-C_3N_4 as efficient catalyst for photocatalytic desulfurization: mechanism, kinetics and influencing factors. Chem Eng J 2017;326:87–98.
[41] Ye L, Wu D, Chu KH, et al. Phosphorylation of g-C_3N_4 for enhanced photocatalytic CO_2 reduction. Chem Eng J 2016;304:376–83.
[42] Liang J, Zheng Y, Chen J, et al. Facile oxygen reduction on a three-dimensionally ordered macroporous graphitic C_3N_4/carbon composite electrocatalyst. Angew Chem Int Ed 2012;51:3892–6.
[43] Wu W, Li X, Ruan Z, et al. Fabrication of a TiO_2 trapped meso/macroporous g-C_3N_4 heterojunction photocatalyst and understanding its enhanced photocatalytic activity based on optical simulation analysis. Inorg Chem Front 2018;5:481–9.
[44] Yan H. Soft-templating synthesis of mesoporous graphitic carbon nitride with enhanced photocatalytic H_2 evolution under visible light. Chem Commun 2012;48:3430–2.
[45] Jiang D, Zhu J, Chen M, et al. Highly efficient heterojunction photocatalyst based on nanoporous g-C_3N_4 sheets modified by Ag_3PO_4 nanoparticles: synthesis and enhanced photocatalytic activity. J Colloid Interface Sci 2014;417:115–20.
[46] Zhao R, Gao J, Mei S, et al. Facile synthesis of graphitic C_3N_4 nanoporous-tube with high enhancement of visible-light photocatalytic activity. Nanotechnology 2017;28:495710.
[47] Feng D, Cheng Y, He J, et al. Enhanced photocatalytic activities of g-C_3N_4 with large specific surface area via a facile one-step synthesis process. Carbon 2017;125:454–63.
[48] Zhao S, Zhang Y, Zhou Y, et al. Facile one-step synthesis of hollow mesoporous g-C_3N_4 spheres with ultrathin nanosheets for photoredox water splitting. Carbon 2018;126:247–56.
[49] Wei H, McMaster WA, Tan JZY, et al. Tricomponent brookite/anatase TiO_2/g-C_3N_4 heterojunction in mesoporous hollow microspheres for enhanced visible-light photocatalysis. J Mater Chem A 2018;6:7236–45.
[50] Hao R, Wang G, Tang HS, et al. Template-free preparation of macro/mesoporous g-C_3N_4/TiO_2 heterojunction photocatalysts with enhanced visible light photocatalytic activity. Appl Catal B Environ 2016;187:47–58.
[51] Li Y, Jiang Y, Ruan Z, et al. Simulation-guided synthesis of graphitic carbon nitride beads with 3D interconnected and continuous meso/macropore channels for enhanced light absorption and photocatalytic performance. J Mater Chem A 2017;5:21300–12.
[52] Xu J, Wang Z, Zhu Y. Enhanced visible-light-driven photocatalytic disinfection performance and organic pollutant degradation activity of porous g-C_3N_4 nanosheets. ACS Appl Mater Interfaces 2017;9:27727–35.
[53] Tong Z, Yang D, Xiao T, et al. Biomimetic fabrication of g-C_3N_4/TiO_2 nanosheets with enhanced photocatalytic activity toward organic pollutant degradation. Chem Eng J 2015;260:117–25.
[54] Dong F, Wu L, Sun Y, et al. Efficient synthesis of polymeric g-C_3N_4 layered materials as novel efficient visible light driven photocatalysts. J Mater Chem 2011;21:15171–4.

[55] Chang F, Xie Y, Li C, et al. A facile modification of g-C_3N_4 with enhanced photocatalytic activity for degradation of methylene blue. Appl Surface Sci 2013;280:967–74.
[56] Yan SC, Li ZS, Zou ZG. Photodegradation performance of g-C_3N_4 fabricated by directly heating melamine. Langmuir 2009;25:10397–401.
[57] Naushad M, Ahamad T, Sharma G, et al. Synthesis and characterization of a new starch/SnO_2 nanocomposite for efficient adsorption of toxic Hg^{2+} metal ion. Chem Eng J 2016;300:306–16.
[58] Epifani M, Alvisi M, Mirenghi L, et al. Sol-gel processing and characterization of pure and metal-doped SnO_2 thin films. J Am Ceram Soc 2001;84:48–54.
[59] Zhang S, Li J, Wang X, et al. In situ ion exchange synthesis of strongly coupled Ag@AgCl/g-C_3N_4 porous nanosheets as plasmonic photocatalyst for highly efficient visible-light photocatalysis. ACS Appl Mater Interfaces 2014;6:22116–25.
[60] Wang XJ, Yang WY, Li FT, et al. In situ microwave-assisted synthesis of porous N-TiO_2/g-C_3N_4 heterojunctions with enhanced visible-light photocatalytic properties. Ind Eng Chem Res 2013;52:17140–50.
[61] Dementjev AP, De Graaf A, Van de Sanden MCM, et al. X-ray photoelectron spectroscopy reference data for identification of the C_3N_4 phase in carbon-nitrogen films. Diamond Relat Mater 2000;9:1904–7.
[62] Bhattacharyya S, Cardinaud C, Turban G. Spectroscopic determination of the structure of amorphous nitrogenated carbon films. J Appl Phys 1998;83:4491–500.
[63] Bhattacharyya S, Hong J, Turban G. Determination of the structure of amorphous nitrogenated carbon films by combined Raman and X-ray photoemission spectroscopy. J Appl Phys 1998;83:3917–9.
[64] Zhang L, Zhao K, Yu R, et al. Phosphorus enhanced intermolecular interactions of SnO_2 and graphene as an ultrastable lithium battery anode. Small 2017;13:1603973–81.
[65] Song H, Zhang L, He C, et al. Graphene sheets decorated with SnO_2 nanoparticles: in situ synthesis and highly efficient materials for cataluminescence gas sensors. J Mater Chem 2011;21:5972–7.
[66] Chen Y, Huang ZH, Yue M, et al. Integrating porphyrin nanoparticles into a 2D graphene matrix for free-standing nanohybrid films with enhanced visible-light photocatalytic activity. Nanoscale 2014;6:978–85.
[67] Xiang Q, Yu J, Jaroniec M. Preparation and enhanced visible-light photocatalytic H_2-production activity of graphene/C_3N_4 composites. J Phys Chem C 2011;115:7355–63.
[68] Vijayan BL, Krishnan SG, Zain NKM, et al. Large scale synthesis of binary composite nanowires in the Mn_2O_3-SnO_2 system with improved charge storage capabilities. Chem Eng J 2017;327:962–72.
[69] Li Y, Jin R, Xing Y, et al. Macroscopic foam-like holey ultrathin g-C_3N_4 nanosheets for drastic improvement of visible-light photocatalytic activity. Adv Energy Mater 2016;6:1601273–78.
[70] Du J, Lai X, Yang N, et al. Hierarchically ordered macro-mesoporous TiO_2-graphene composite films: improved mass transfer, reduced charge recombination, and their enhanced photocatalytic activities. ACS Nano 2011;5:590–6.
[71] Chen Y, Li A, Huang ZH, et al. Porphyrin-based nanostructures for photocatalytic applications. Nanomaterials 2016;6:51–68.
[72] Chen Y, Zhang C, Zhang X, et al. One-step growth of organic single-crystal p-n nano-heterojunctions with enhanced visible-light photocatalytic activity. Chem Commun 2013;49:9200–2.
[73] Yin R, Luo Q, Wang D, et al. SnO_2/g-C_3N_4 photocatalyst with enhanced visible-light photocatalytic activity. J Mater Sci 2014;49:6067–73.

Yingzhi Chen is an Associate Professor in School of Materials Science and Engineering, University of Science and Technology Beijing, China. She received her B.S. (2007) degree from Beijing Normal University, Ph.D. (2012) degree in Technical Institute of Physics and Chemistry, Chinese Academy of Sciences. Her research mainly focuses on the design, fabrication of optoelectronic compounds & devices, as well as novel biomedical materials.

Zheng-Hong Huang is a Professor in School of Materials Science and Engineering, Tsinghua University, China. He received his B.S. (1992) degree from Wuhan University of Technology in China, M.S. (1995) degree in Zhejiang University and Ph.D. (2002) degree from Tsinghua University. His research interests focus on carbon materials related to environmental protection and energy issues, including (1) new carbon materials; (2) adsorbents and photocatalyst for removing gaseous and aqueous contaminants; (3) carbon materials for electrodes of lithium-ion batteries and supercapacitors.

Lu-Ning Wang is a Thousand Youth Talent, Professor and Dean of the School of Materials Science and Engineering, University of Science and Technology Beijing, China. He received his B.S. (2002) degree from University of Science and Technology Beijing, M.S. (2005) degree in Tsinghua University, and Ph.D. (2011) degree from University of Alberta in Canada. His research mainly focuses on the design, preparation, theoretical study of novel biomedical materials.